# High-resolution Study of the Outflow Activity and Chemical Environment of Chamaeleon-MMS1

Downloaded from: https://research.chalmers.se, 2026-10-16 15:28 UTC

Citation for the original published paper (version of record):

Allen, V., Cordiner, M., Adande, G. et al (2024). High-resolution Study of the Outflow Activity and Chemical Environment of Chamaeleon-MMS1. Astrophysical Journal, 971(2). http://dx.doi.org/10.3847/1538-4357/ad5182

N.B. When citing this work, cite the original published paper.

research.chalmers.se offers the possibility of retrieving research publications produced at Chalmers University of Technology. It covers all kind of research output: articles, dissertations, conference papers, reports etc. since 2004. research.chalmers.se is administrated and maintained by Chalmers Library

(article starts on next page)

The Astrophysical Journal, 971:187 (13pp), 2024 August 20 https://doi.org/10.3847/1538-4357/ad5182
© 2024. The Author(s). Published by the American Astronomical Society.
OPEN ACCESS

# High-resolution Study of the Outflow Activity and Chemical Environment of Chamaeleon-MMS1

Veronica Allen[1,2,7,8], Martin A. Cordiner[2,3], Gilles Adande[2,8], Steven B. Charnley[2], Yi-Jehng Kuan[4,5], and Eva Wirström[6]
[1] Kapteyn Astronomical Institute, University of Groningen 9747 AD Groningen, The Netherlands; allen@astro.rug.nl
[2] Astrochemistry Laboratory, NASA Goddard Space Flight Center 8800 Greenbelt Road, Greenbelt, MD 20771, USA
[3] Institute for Astrophysics and Computational Sciences, The Catholic University of America, Washington, DC 20064, USA
[4] Department of Earth Sciences, National Taiwan Normal University, Taipei 11677, Taiwan, ROC
[5] Institute of Astronomy and Astrophysics, Academia Sinica Taipei, 10617, Taiwan, ROC
[6] Department of Space, Earth, and Environment, Chalmers University of Technology Onsala Space Observatory, 439 92 Onsala, Sweden
*Received 2023 March 30; revised 2024 May 25; accepted 2024 May 27; published 2024 August 20*

## Abstract

The earliest stages of low-mass star formation are unclear, with the first hydrostatic core (FHSC) as the transition stage between a prestellar and protostellar core. This work describes the local (∼4000 au) outflow activity associated with candidate FHSC Chamaeleon-MMS1 and its effect on the surrounding material to determine the evolutionary state of this young low-mass source. We observed Chamaeleon-MMS1 with the Atacama Large Millimeter/submillimeter Array at 220 GHz at high spatial (∼75 au) and spectral resolutions (0.1–0.3 km s$^{-1}$). A low-energy outflow is detected, consisting of two components, a broad spectral feature ($\Delta v \sim 8$ km s$^{-1}$) to the northeast and narrow spectral features ($\Delta v \sim 1$ km s$^{-1}$) to both the northeast and southwest. The molecular tracers CS, formaldehyde ($H_2CO$), and methanol ($CH_3OH$) were used to analyze the effect of the outflows on the surrounding gas and determine its rotational temperature. The rotational temperature of $H_2CO$ is 40 K toward the continuum source with similarly low temperatures (10–75 K) toward clumps affected by the outflow. $CH_3OH$ is only detected toward gas clumps located away from the continuum source, where the methanol is expected to have been released by the energy of the outflow through ice sputtering. While molecular emission and high outflow speeds rule Cha-MMS1 out as an FHSC, its outflow is less energetic than those of other Class 0 objects and its physical properties are within the range covered by other low-luminosity protostars. The inferred gas temperatures toward the continuum source are also relatively low, indicating that Cha-MMS1 is one of the youngest known sources.

*Unified Astronomy Thesaurus concepts:* Stellar jets (1607); Astrochemistry (75); Star formation (1569); Low mass stars (2050); Young stellar objects (1834); CO line emission (262); Millimeter astronomy (1061); Interferometry (808)

## 1. Introduction

Understanding star formation is a central problem in astrophysics, with direct implications for our understanding of how galaxies evolve and how planets and life form. Stars form in collapsing cores, corresponding to the densest regions within molecular clouds, but the precise details of this process are still far from being completely understood, particularly during the initial collapse period. Hydrodynamic and magnetohydrodynamic simulations of a molecular cloud undergoing gravitational collapse (Larson 1969; Masunaga & Inutsuka 2000; Machida et al. 2008; Tomida et al. 2010, 2015; Masson et al. 2016; Bhandare et al. 2018; Young 2023) show that the collapse is arrested by thermal pressure once the density ($n$) becomes sufficiently great that cooling by dust radiation is inhibited (at $n \gtrsim 10^{11}$ cm$^{-3}$). At this point, a quasi-hydrostatic object is formed, known as the first hydrostatic core (FHSC). The FHSC is calculated to persist in an approximately adiabatic state for $\sim 10^3$ yr, which is a sufficiently short time to make it a rare object in nearby star-forming regions (Young 2023). These sources are expected to be relatively cold (a few hundred Kelvins) and compact (∼5–20 au radius), providing a challenge for detection and classification (Bate et al. 2014). Observational signatures of the FHSC include a low luminosity (∼0.01–0.1 $L_\odot$), and an approximately thermal spectral energy distribution that peaks in the far-infrared/submillimeter range (Saigo & Tomisaka 2011). A low-luminosity source is generally considered to be an FHSC candidate if it shows little to no emission at wavelengths $\leqslant 70$ $\mu$m. Calculations show that the FHSC should also produce a slow molecular outflow, which extends up to a distance of a few hundred astronomical units from the core (Machida et al. 2008; Tomida et al. 2010). Typically, slow uncollimated outflows are expected, but Price et al. (2012) demonstrated that collimated jets with velocities up to 7 km s$^{-1}$ are possible during the FHSC phase.

Characterizing Very Low-Luminosity Objects (VeLLOs) has proven to be challenging over the past 15 years (Dunham et al. 2008), with the number of identified FHSC candidates decreasing as they are studied in depth and reclassified. Currently, the remaining FHSC candidates are NGC 1333-IRAS 4C (Koumpia et al. 2016), L1535-NE/MC35-mm (Fujishiro et al. 2020), Oph A N6 and Oph A SM1 (Friesen et al. 2018), G208.89-20. (Dutta et al. 2022), and perhaps Per-Bolo 45 (Maureira et al. 2020). The list of very low-luminosity class 0 protostars includes IRAS 15398-3359 (Okoda et al. 2020), L673-7 IRS (Dunham et al. 2011), L1014-IRS (Dunham et al. 2011), L1148-IRS

[7] NWO Veni Fellow.
[8] NASA Postdoctoral Program fellow.

Original content from this work may be used under the terms of the Creative Commons Attribution 4.0 licence. Any further distribution of this work must maintain attribution to the author(s) and the title of the work, journal citation and DOI.

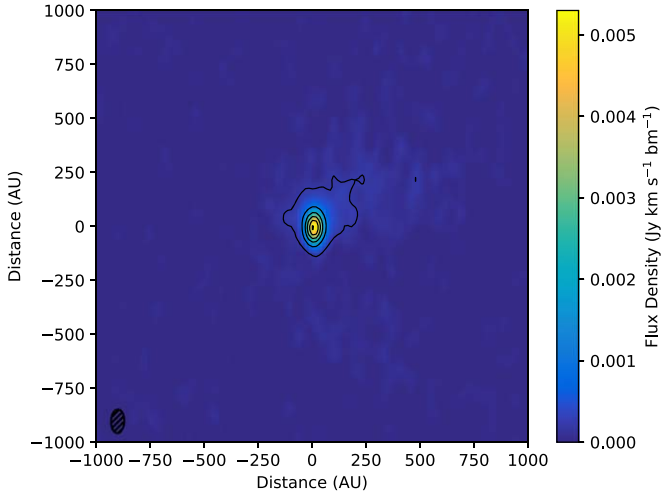


**Figure 1.** 220 GHz continuum map of Cha-MMS1. Contours start at 3$\sigma$ (with an rms of 0.21 mJy beam$^{-1}$) continue at 1.05, 2.10, 3.15, 4.20, and 5.25 mJy beam$^{-1}$ with a peak of 6.48 mJy beam$^{-1}$. The beam size is 0.″72 × 0.″41.

**Table 1**
Targeted Spectral Lines ($E_{up}$ and $A_{ij}$ from CDMS)

| Species | Transition | Frequency (GHz) | $E_{up}$ (K) | log ($A_{ij}$) |
|---|---|---|---|---|
| CO | 2-1 | 230.5380 | 16.6 | −6.16 |
| $^{13}$CO | 2-1 | 220.3986 | 15.9 | −6.22 |
| CS | 5-4 | 244.9355 | 35.3 | −3.53 |
| $H_2CO$ | $3_{0,3}$-$2_{2,1}$ | 218.2221 | 20.9 | −3.55 |
| $H_2CO$ | $3_{2,2}$-$2_{2,1}$ | 218.4756 | 68.1 | −3.80 |
| $H_2CO$ | $3_{1,2}$-$2_{1,1}$ | 225.6977 | 33.4 | −3.56 |
| $CH_3OH$ | $5_{3,2}$-$4_{3,1}$ | 218.4400 | 45.5 | −4.33 |
| $CH_3OH$ | $5_{-1,5}$-$4_{-1,4}$ | 241.7672 | 40.4 | −4.24 |
| $CH_3OH$ | $5_{0,5}$-$4_{0,4}$++ | 241.7914 | 34.8 | −4.22 |
| $HC_3N$ | 24-23 | 218.3247 | 131.0 | -3.08 |

(Dunham et al. 2011), L1451-mm (Pineda et al. 2011), GSS30, SM1N, B2-A7, and IRAS 16267-2417 in Oph A (Friesen et al. 2018), as well as sources formerly identified as FHSC candidates: Per-Bolo 58 (Maureira et al. 2020), B1b-N (Marcelino et al. 2018), and B1b-S (Hirano 2019). Other VeLLOs have subsequently been identified as either prestellar objects, for example CB17-MMS (Spear et al. 2021), or found not to be star-forming cores, as in the case of L1448 IRS 2E (Maureira et al. 2020).

Chamaeleon-MMS1 (Cha-MMS1) is within the Chamaeleon I molecular cloud complex located at a distance of 192 pc (Dzib et al. 2018) with a systemic velocity of 4.5 km s$^{-1}$ (Belloche et al. 2006) and was first detected in 1.3 mm emission by Reipurth et al. (1996). The central object is deeply embedded inside a dense molecular cloud (Cordiner et al. 2012) and has been classified by Belloche et al. (2006, 2011) as either an extremely young VeLLO or an FHSC with an internal luminosity between 0.08 and 0.18 $L_\odot$ (Tsitali et al. 2013). Belloche et al. (2006) did not find any evidence of CO outflow activity from Cha-MMS1 using single-dish (APEX) observations, and the studies of Hiramatsu et al. (2007) and Ladd et al. (2011) determined that the nearby HH 49/50 outflow is driven by the more evolved Class I protostar Ced 110 IRS 4. Ladd et al. (2011) determined from single-dish CO observations that the IRS 4 outflow is deflected around (or grazes the edge of) the 100″-diameter dense clump that contains the collapsing protostar Cha-MMS1. Väisälä et al. (2014) analyzed $NH_3$ and continuum emission toward Cha-MMS1 using the Australia Telescope

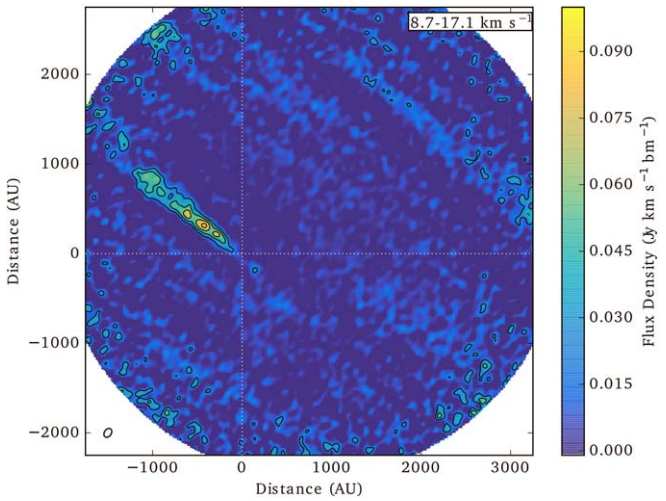


**Figure 2.** Primary beam-corrected integrated intensity map (between 8.7 and 17.1 km s$^{-1}$) of broad component of CO outflow. Contours start at 3$\sigma$ (rms of 7 mJy beam$^{-1}$ km s$^{-1}$) continue in intervals of 3$\sigma$ to a peak of 91 mJy beam$^{-1}$ km s$^{-1}$. The beam size is 0.″72 × 0.″52.

Compact Array (ATCA) and concluded that a warm central source was within, but it was at the Class 0 stage at the latest. Recently, Busch et al. (2020) published an analysis of the CO(3-2) emission tracing the outflow activity associated with Cha-MMS1 and concluded that it is at a stage later than the FHSC based on the high outflow velocities. The outflow in that article is qualitatively similar to the CO(2-1) emission in this work, but we also present the outflow activity as traced by CS, $H_2CO$, and $CH_3OH$, showing different structures than those traced by the CO observation. Additionally, analysis of multiple FHSC candidates (including Cha-MMS1) using dense envelope tracers was published by Maureira et al. (2020). Both studies conclude that Cha-MMS1 is at a very young evolutionary state.

In this paper, we present the high angular resolution analysis of the outflow activity associated with Cha-MMS1 and their effect on the surrounding material. In Section 2, we give details of the Atacama Large Millimeter/submillimeter Array (ALMA) observations and data reduction. Section 3 contains the details of five detected species including isotopologs (CO, $^{13}$CO, CS, $H_2CO$, and $CH_3OH$), analysis of the outflow mechanical properties, and determination of the rotational temperature of various subregions in this source. In Section 4, we discuss the implications of our results, and in Section 5 we present our conclusions regarding the nature of this extremely young protostellar object.

## 2. Observations and Data Reduction

Cha-MMS1 was observed using the ALMA on 2014 July 16 and 2015 June 6 and 7 using 26 antennas on July 16, and 37–39 antennas on June 6 and 7 (project code 2013.1.01113.S) with an angular resolution of ∼0.″7 and spectral resolutions of ∼0.08 km s$^{-1}$ in three spectral windows (covering $^{12}$CO, $^{13}$CO, and CS), 0.17 km s$^{-1}$ for $H_2CO$ (218222 MHz), and 0.3 km s$^{-1}$ in the other four spectral windows. The observations were conducted in configuration 4 with a maximum recoverable scale (MRS) of 5.″7. The calibrators used were Callisto, Ganymede, J0635-7516, J1058-8003, J1208-7809, J1107-4449, and J0538-4405. The pointing position of our ALMA observations was the millimeter position reported in Reipurth et al. (1996) rather than the Spitzer IR peak, therefore the source is consistently offset in our maps. Data reduction was performed with the CASA package

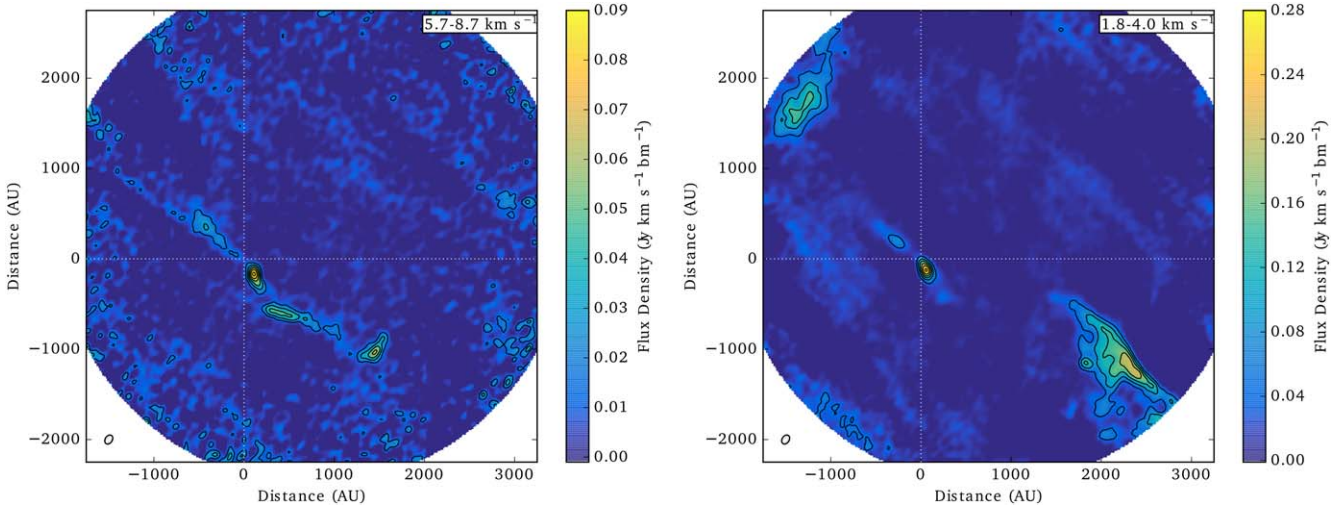


**Figure 3.** Primary beam-corrected integrated intensity maps for $^{12}$CO narrow emission features. The continuum peak is located at (0, 0) au and is indicated by the intersection of the dotted lines. The beam size is 0.″72 × 0.″52. Left: integrated intensity map (between 5.7 and 8.7 km s$^{-1}$) of narrow redshifted component of CO outflow. Contours start at 3$\sigma$ (rms of 4.8 mJy beam$^{-1}$ km s$^{-1}$) continue in intervals of 3$\sigma$ to a peak of 94 mJy beam$^{-1}$ km s$^{-1}$. Right: integrated intensity map (between 1.8 and 4.0 km s$^{-1}$) of narrow blueshifted lobes of CO outflow. Contours start at 3$\sigma$ (rms of 15 mJy beam$^{-1}$ km s$^{-1}$) and continue in intervals of 3$\sigma$ up to a peak of 277 mJy beam$^{-1}$ km s$^{-1}$.

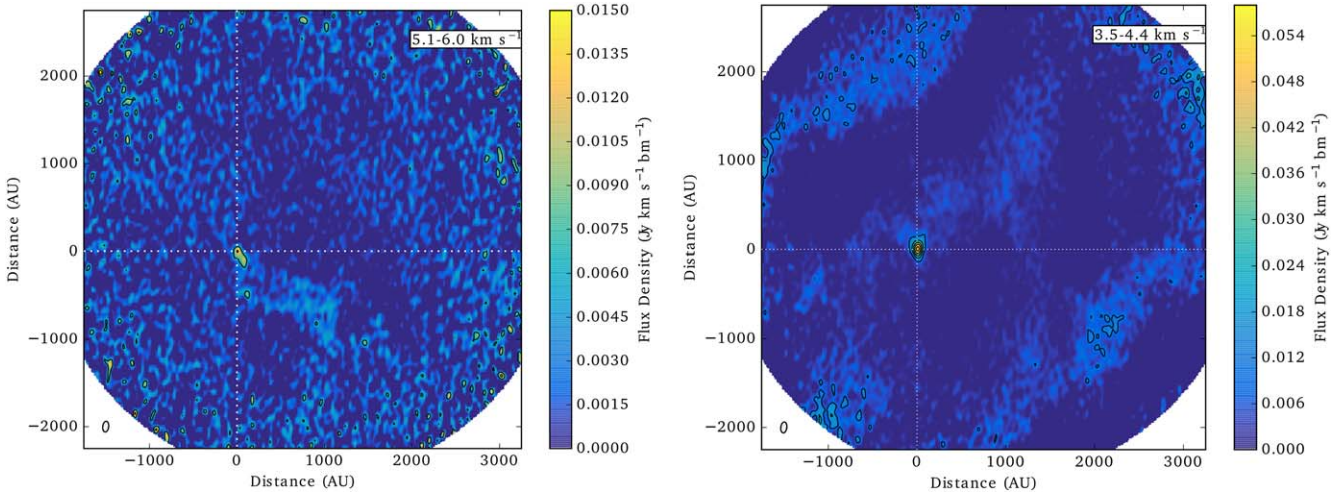


**Figure 4.** Primary beam-corrected integrated intensity maps for $^{13}$CO emission features. The continuum peak is located at (0, 0) au and is indicated by the intersection of the dotted lines. The beam size is 0.″82 × 0.″45 Left: integrated intensity map (between 5.1 and 6.0 km s$^{-1}$) of red component of $^{13}$CO outflow. Contours start at 3$\sigma$ (rms of 2.1 mJy beam$^{-1}$ km s$^{-1}$) and continue in intervals of 3$\sigma$ to a peak of 13.7 mJy beam$^{-1}$ km s$^{-1}$. Right: integrated intensity map (between 3.5 and 4.4 km s$^{-1}$) of blue component of $^{13}$CO outflow. Contours start at 3$\sigma$ (rms of 4.3 mJy beam$^{-1}$ km s$^{-1}$) and continue in intervals of 3$\sigma$ to a peak of 56.7 mJy beam$^{-1}$ km s$^{-1}$.

(version 5.4.0). Corresponding spectral windows from different observation dates were concatenated and the continuum was subtracted. Imaging was done using the tclean process with a Hogbom deconvolver and Briggs weighting with a robust parameter of 0.5 and all images are primary beam corrected. The rms noise for line-free channels was typically 2–4 mJy.

## 3. Results

### 3.1. Continuum and Line Detection

Figure 1 shows the compact, unresolved, continuum emission at 220 GHz detected toward Cha-MMS1. Our observations targeted several molecular species expected in very young low-mass star-forming regions, as summarized in Table 1. $^{12}$CO emission is resolved out on large scales, but a weak spectral feature covering the broad velocity range of 8.7–17.1 km s$^{-1}$ is detected in $^{12}$CO to the northeast of the continuum source (Section 3.2.1, Figure 2). Moment maps were also made of narrow spectral features in $^{12}$CO and $^{13}$CO (Section 3.2.2, Figures 3 and 4). There is absorption in both $^{12}$CO and $^{13}$CO with no signal for each in the ranges 4.0–5.7 km s$^{-1}$ and 4.4–5.1 km s$^{-1}$, respectively. $^{13}$CO shows strong emission toward the continuum source and weak emission (less than 3$\sigma$) cospatial with the narrow red $^{12}$CO emission southwest of the continuum source. CS emission is clumpy and, on larger spatial scales, the CS clumps seem to trace out a cone (Section 3.3, Figure 6). Within 1.″5 (288 au) of the continuum source spectral emission of CS shows an hourglass-like morphology. Three $H_2CO$ lines were detected (Section 3.4, Figure 16) showing emission in different regions, most of which correspond with the locations of CS emission. Three weak $CH_3OH$ transitions were detected at 5–10$\sigma$ rms levels (Section 3.5) coinciding with the $H_2CO$ emission but not coincident with the compact continuum emission from Cha-MMS1. The targeted $HC_3N$ transition was not detected. Spectra from different areas of Cha-MMS1 can be found

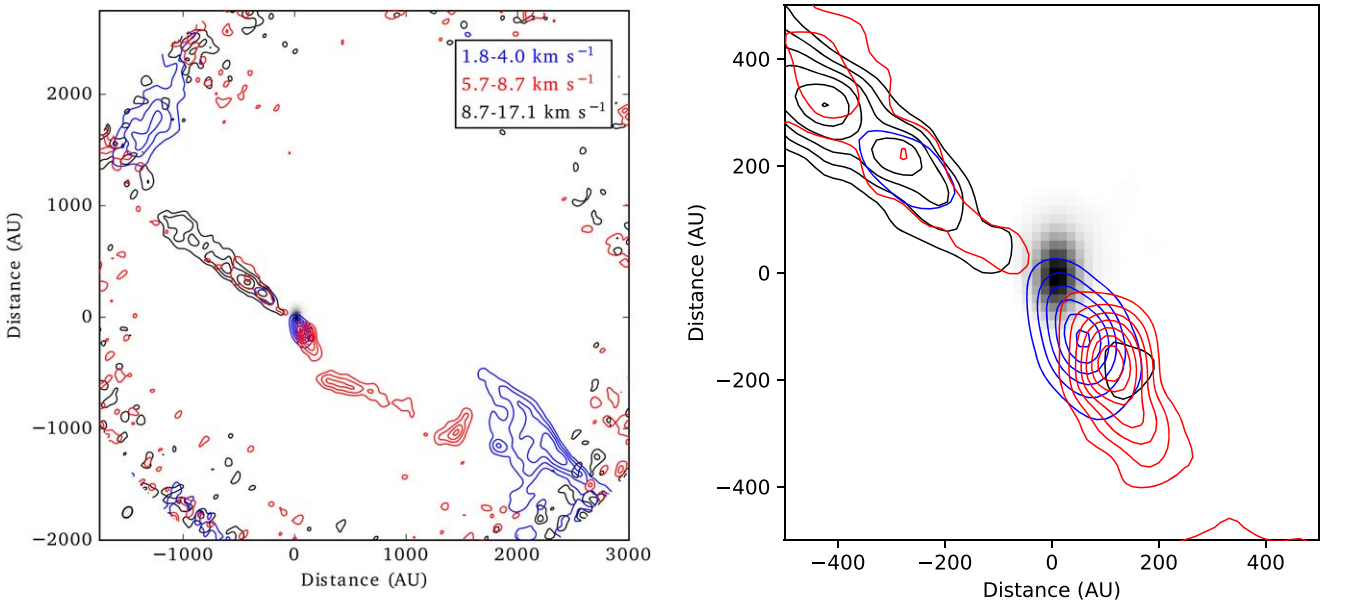


**Figure 5.** Primary beam-corrected integrated intensity image of the $^{12}$CO emission over the redshifted, narrow velocity range from 5.7 to 8.7 km s$^{-1}$ (red contours) and the blueshifted, narrow velocity range from 1.8 to 4.0 km s$^{-1}$ (blue contours). The $^{12}$CO emission of the redshifted, broad velocity range from 8.7 to 17.1 km s$^{-1}$ is shown in black contours and all are overlaid on the continuum emission of Cha-MMS1 (grayscale). Contours are as in Figures 2 and 3. The left figure shows the full extent of the emission and the right figure shows the detail of the inner 1000 au. The beam size is 0.″72 × 0.″52.

**Table 2**
Calculated Mechanical Outflow Properties from CO Emission (Errors in Parentheses) Assuming $\tau = 5$

| | Northern Red | Southern Red | Northern Blue | Southern Blue | Predicted |
|---|---|---|---|---|---|
| $V_{max}$ (km s$^{-1}$) | 12.4 (0.1) | 4.0 (0.1) | 3.2 (0.1) | 2.9 (0.1) | [a] |
| $V_{dep}$ (km s$^{-1}$) | 71.8 (0.6) | 23.4 (0.6) | 18.6 (0.6) | 16.8 (0.6) | [a] |
| $t_{dyn}$ (yr) | 130 (10) | 490 (20) | 720 (20) | 800 (30) | [a] |
| Outflow mass ($M_\odot$) | 5.2 (1.0) × 10$^{-5}$ | 7.4 (1.7) × 10$^{-5}$ | 4.7 (0.6) × 10$^{-5}$ | 2.1 (0.1) × 10$^{-4}$ | 2.2–3.5 × 10$^{-2}$ |
| Mass-loss rate ($M_\odot$ yr$^{-1}$) | 4.1 (1.2) × 10$^{-7}$ | 1.5 (0.4) × 10$^{-7}$ | 3.3 (0.7) × 10$^{-7}$ | 3.1 (0.3) × 10$^{-7}$ | [a] |
| Momentum ($M_\odot$ km s$^{-1}$) | 3.7 (0.8) × 10$^{-3}$ | 1.7 (0.4) × 10$^{-3}$ | 9.9 (1.2) × 10$^{-4}$ | 9.4 (0.7) × 10$^{-3}$ | [a] |
| Kinetic energy (erg) | 2.6 (0.5) × 10$^{42}$ | 4.0 (0.9) × 10$^{41}$ | 1.6 (1.9) × 10$^{41}$ | 5.9 (0.4) × 10$^{41}$ | [a] |
| Mechanical luminosity ($L_\odot$) | 1.1 (2.7) × 10$^{-1}$ | 5.7 (3.1) × 10$^{-3}$ | 2.3 (0.8) × 10$^{-3}$ | 2.4 (0.2) × 10$^{-2}$ | 2.2–3.6 × 10$^{-3}$ |
| Momentum rate ($M_\odot$ km s$^{-1}$ yr$^{-1}$) | 2.9 (0.7) × 10$^{-5}$ | 3.6 (1.4) × 10$^{-6}$ | 1.4 (0.1) × 10$^{-6}$ | 1.1 (0.1) × 10$^{-5}$ | 2.2-4.0 × 10$^{-6}$ |

**Notes.** $V_{max}$ is the observed maximum velocity wrt $V_{LSR}$. $V_{dep}$ is the deprojected maximum velocity taking into account the outflow direction, Velocity-dependent properties are calculated based on the deprojected velocity assuming an inclination of 80°. Derived value ranged based on the trends in Wu et al. (2004) for a young star with an $L_{bol}$ of 0.08–0.18 $L_\odot$ are stated in the column "Predicted."
[a] Nonderivable velocity-based properties.

in Appendix A where Figure 11 shows the spectral extraction regions, Figures 12 and 13 show the spectra for CO, Figure 14 shows spectra for $H_2CO$, and Figure 15 shows spectra for $CH_3OH$.

### 3.2. Outflow Activity

The emission detected in $^{12}$CO was used to determine the properties of outflow activity associated with this source. Both the red and blue lobes of the narrow outflow component are located toward the northeast and southwest of the continuum source with an additional spectrally broad red component appearing to the northeast.

#### 3.2.1. $^{12}$CO High-velocity Outflow Components

A weak, broad redshifted outflow is detected to the northeast of the continuum source in $^{12}$CO (Figure 2). It is quite collimated with a collimation factor of 5.5. A Gaussian fit made to this component of the $^{12}$CO emission shows that the center is at $10.9 \pm 0.2$ km s$^{-1}$ and the full-width half-maximum (FWHM) is $6.7 \pm 0.4$ km s$^{-1}$. The blue counterpart to the southwest is not nearly as broad or collimated (see Figure 3 right). A Gaussian fit of the southern blue component has a central velocity of $3.40 \pm 0.01$ km s$^{-1}$ and a FWHM of $0.77 \pm 0.03$ km s$^{-1}$. This much narrower spectral line may not be the opposite component of the broad red outflow, but no similarly broad blue component was detected. No broad component is detected in $^{13}$CO (Figure 4).

#### 3.2.2. $^{12}$CO and $^{13}$CO Low-velocity Bipolar Components

The left frames of Figures 3 and 4 show $^{12}$CO and $^{13}$CO integrated intensity maps (between 5.7 and 8.7 km s$^{-1}$ and 5.1 and 6.0 km s$^{-1}$, respectively) of spectrally narrow redshifted outflow activity to the south of the continuum source which coincide in an "S"-like shape. The blue components of $^{12}$CO (Figure 3 right) are both to the northeast and southwest at the edges of the field of view. These blue components appear to be the ends of the outflow, but as we do not have a larger field of- view, we

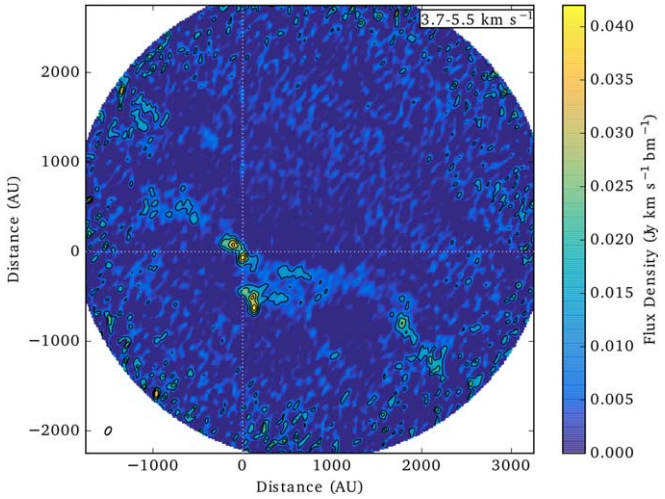


**Figure 6.** Primary beam-corrected integrated intensity map (between 3.7 and 5.5 km s$^{-1}$) of CS emission. The continuum peak is located at (0, 0) au and is indicated by the intersection of the dotted lines. Contours start at 3$\sigma$ (rms of 9 mJy beam$^{-1}$ km s$^{-1}$) continue in intervals of 3$\sigma$ to a peak of 42.2 mJy beam$^{-1}$ km s$^{-1}$. The beam size is 0.″65 × 0.″39.

cannot confirm this. The line profiles of the $^{12}$CO components have narrow FWHM at $1.4 \pm 0.1$ km s$^{-1}$ (southern red) and $0.72 \pm 0.07$ km s$^{-1}$ (northern blue) with central peaks near $v_{LSR}$ of Cha-MMS1 at $6.94 \pm 0.04$ km s$^{-1}$ and $3.55 \pm 0.03$ km s$^{-1}$. The spectral lines for $^{13}$CO have even narrower FWHM at $0.34 \pm 0.02$ km s$^{-1}$ and $0.35 \pm 0.01$ km s$^{-1}$ with central peaks at $5.47 \pm 0.01$ km s$^{-1}$ and $3.565 \pm 0.006$ km s$^{-1}$ for the red and blue lobes, respectively. All three components of the $^{12}$CO outflow—broad red, narrow red, and narrow blue—are shown in Figure 5. Details of the spectra across the region can be found in Appendix A in Figures 12 and 13.

#### 3.2.3. Mechanical Outflow Properties

We used the approach described in Sánchez-Monge et al. (2013) and López-Sepulcre et al. (2009) to calculate the mechanical outflow properties. The measured properties for each outflow lobe are the difference between the maximum velocity and systemic velocity ($v_{max}$), the length of the major axis (at the 5$\sigma$ contour), the area of the outflow (as an ellipse), and the integrated intensity of the emission between $v_{max}$ and 2$\sigma$ from the line peak ($\int T_{mb} dv$). The CO column density was determined assuming optically thin emission as in Goldsmith & Langer (1999, Equations (10) and (19)), assuming excitation temperatures of 10, 20, and 30 K. The calculated CO column densities varied by a factor of 3–4 between the different temperatures, so we used the average for calculating the hydrogen column density ($N_{H2}$) assuming a CO abundance of $10^{-4}$, as is typical (Bolatto et al. 2013). Because the CO emission showed strong self-absorption at velocities near the velocity of the system ($v_{LSR} = 4.9$ km s$^{-1}$), the CO intensities were corrected assuming an $\tau$ value of 5.

The other calculated properties are: outflow mass (calculated using the area of the outflow lobe and the mass of the hydrogen from the calculated $H_2$ column density), the dynamical or kinetic time $t_{dyn}$ (the length of the outflow lobe divided by $v_{max}$), kinetic energy (outflow mass times 0.5 $v_{max}^2$), momentum (outflow mass times $v_{max}$), momentum rate, which is also called the force (momentum/$t_{dyn}$), mass-loss rate (outflow mass/$t_{dyn}$), and mechanical luminosity (kinetic energy/$t_{dyn}$). As the direction of the outflow is near the plane of the sky, we applied the inclination correction factors from López-Sepulcre et al. (2010) assuming an inclination of 80°. We determined this inclination geometrically taking into account the opening angle of the northern red outflow and the presence of red and blue components in each direction.

The mechanical outflow properties are summarized in Table 2 for the detected outflow lobes. The fast broad outflow component (northern red) has a maximum relative velocity of ∼12 km s$^{-1}$ (deprojected to ∼70 km s$^{-1}$). The narrow components have a maximum velocity of ∼4 km s$^{-1}$ (deprojected to ∼20 km s$^{-1}$). Using the trends outlined in Wu et al. (2004), we calculated the momentum rate, outflow mass, and mechanical luminosity expected from a young star with an $L_{bol}$ of 0.08–0.18 $L_\odot$. The momentum rate would be $2.2–4.0 \times 10^{-6}$ $M_\odot$ km s$^{-1}$ yr$^{-1}$, the outflow mass $2.2–3.5 \times 10^{-2}$ $M_\odot$, and the mechanical luminosity $2.2–3.6 \times 10^{-3}$ $L_\odot$. The outflow lobes described in this paper have a mass 100–1000 times lower, and a momentum rate and mechanical luminosity comparable to the predicted value from Wu et al. (2004).

### 3.3. CS

Figure 6 shows CS emission tracing a wide cone on larger scales, indicating the interaction between multiple outflows and the surroundings or a steep precessing angle of a single outflow. Alternatively, this morphology could be due to a spatially wider and low-velocity component tracing the cavity walls, as is commonly found toward other protostellar outflows (e.g., Benedettini et al. 2013; Zhang et al. 2018; Okoda et al. 2020). On smaller scales, the CS emission is hourglass shaped and the first moment (velocity) maps (Figure 7) show inverse velocity gradients immediately above and below the continuum source.

### 3.4. $H_2CO$ Emission

$H_2CO$ emission is detected toward the continuum as well as about 3″ (∼600 au) to the south of the continuum source, about 16″ (3100 au) southwest of the continuum source, and 7.″5 (1500 au) northeast of the continuum source in all three detected transitions. We labeled these regions Main (M), south (S), west (W), and north (N) (See Figure 8). The emission from $H_2CO$ in these four regions coincides with CS emission in all cases, but does not show the hourglass morphology toward the central source (Main) seen in CS. Cha-MMS1 W corresponds to the south-western lobe of the CO outflow emission. There is emission detected from the $H_2CO$ transition at 218.222 GHz ($E_{up} = 20.9$ K) about 10″ (1900 au) north–northeast of the continuum source, but the emission detected in this area from the other two transitions is very weak. The higher energy $H_2CO$ transition at 218.475 GHz ($E_{up} = 68$ K) shows very weak emission in each region (see Appendix A Figure 14 for spectra and Appendix B Figure 16 for moment zero maps of all detected transitions).

Table 3 shows the rotational temperatures and column densities determined using the $H_2CO$ transitions in a rotational diagram in the CASSIS software[9] and the CDMS database. Rotational temperatures range from ∼11 K to 73 K with a temperature of 40.4 ($^{+2.7}_{-2.4}$) K toward the continuum source. The column densities are consistently $\sim 10^{13}$ cm$^{-2}$. The gas in these condensations appears to be sufficiently dense for the rotational temperature, gas temperature, and dust temperature to be equal ($n > 10^{4.5}$ cm$^{-3}$; Goldsmith 2001). We discuss the origin of the $H_2CO$ and CS emission in Section 4.2.2.

[9] http://cassis.irap.omp.eu (Vastel et al. 2015). CASSIS has been developed by IRAP-UPS/CNRS.

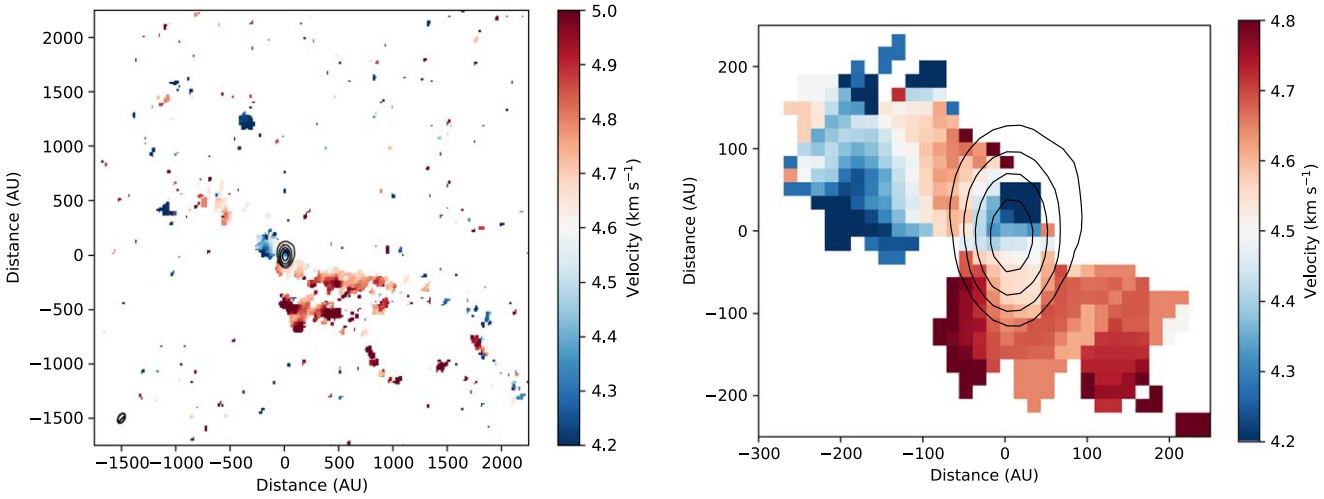


**Figure 7.** Colored pixels correspond to the velocity at each point. The black contours show the continuum source. Left: first moment map (velocity) of CS emission across the field of view. Right: as in left, but focused on emission near the continuum source.

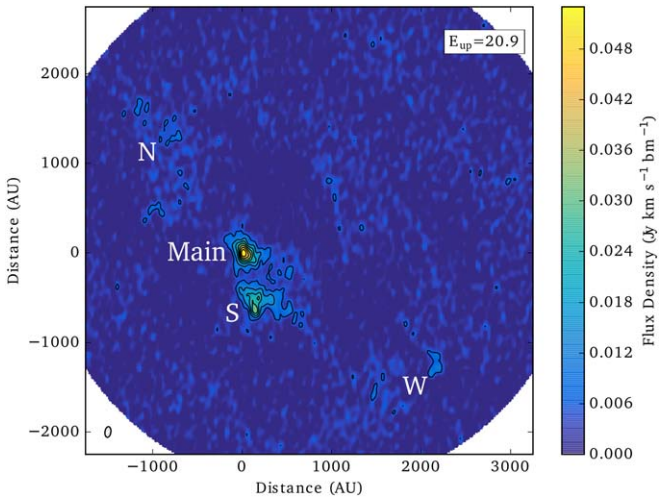


**Figure 8.** Primary beam-corrected integrated intensity map (between 3.1 and 5.5 km s$^{-1}$) for $H_2CO$ transitions at 218.222 GHz ($E_{up} = 20.9$ K). The continuum peak is at 0, 0 au. Contours start at $3\sigma$ (rms of 6 mJy beam$^{-1}$ km s$^{-1}$) continue in intervals of $3\sigma$ to a peak of 53 mJy beam$^{-1}$ km s$^{-1}$. The beam size is 0.″80 × 0.″43.

**Table 3**
$H_2CO$ Gas Properties in Different Regions of Cha-MMS1 with Errors in Parentheses

| Region | $T_{rot}$ (K) | $N_{col}$ (cm$^{-2}$) |
|---|---|---|
| Main | 40.4 (+2.7, −2.4) | 3.8 (0.4) × $10^{13}$ |
| N | 73 (+101, −27) | 2.8 (+0.08, −0.01) × $10^{13}$ |
| S | 10.8 (+0.3, −0.2) | 1.4 (0.1) × $10^{13}$ |
| W | 36.5 (+7.0, −5.1) | 3.9 (+1.2, −0.9) × $10^{13}$ |

**Note.** Note that the fit for N was poor due to the low flux of the transition at 219475 MHz ($E_{up} = 68$ K).

### 3.5. $CH_3OH$ Emission

$CH_3OH$ emission is detected toward the clumps associated with $H_2CO$ emission toward N, S, and W, but not toward Main (Figure 9). All $CH_3OH$ emission lines are much weaker than in other detected species. The brightest of these is the transition at

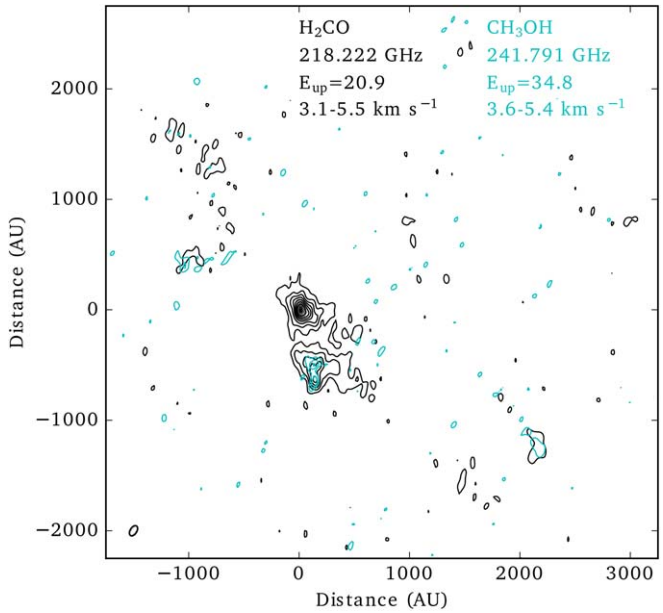


**Figure 9.** Primary beam-corrected integrated intensity maps for $H_2CO$ (218.222 GHz) and $CH_3OH$ (241.791 GHz). Black contours show $H_2CO$ as in Figure 8. Cyan $CH_3OH$ contours (integrated between 3.6 and 5.4 km s$^{-1}$) start at $3\sigma$ (rms of 6.6 mJy beam$^{-1}$ km s$^{-1}$) and continue in $1\sigma$ intervals to a peak of 25 mJy beam$^{-1}$ km s$^{-1}$. The continuum is shown in grayscale coincident with $H_2CO$ emission, but not $CH_3OH$.

**Table 4**
$CH_3OH$ Gas Properties in Different Regions of Cha-MMS1

| Region | $T_{rot}$ (K) | $N_{col}$ (cm$^{-2}$) |
|---|---|---|
| Main | 50[a] | <1.2 × $10^{13}$ |
| N | 41.2 (30.8) | 8.6 (6.4) ×$10^{13}$ |
| S | 23.2 (2.3) | 4.8 (0.8) ×$10^{13}$ |
| W | 15.7 (1.9) | 1.1 (0.4) ×$10^{14}$ |

**Note.**
[a] The rotational temperature of $CH_3OH$ toward Main was assumed to be 50 K to be comparable to the rotational temperature of $H_2CO$ there and the column density is therefore an upper limit.

241.791 GHz ($E_{up} = 34.8$ K), but the other transitions at 241.767 GHz ($E_{up} = 40.4$ K) and 218.440 GHz ($E_{up} = 45.5$ K) are also visible in the images and spectra at greater than $3\sigma$ (see Figures 15 and 17 in the Appendices A and B). The column densities are consistent between regions at $10^{13}$–$10^{14}$ cm$^{-2}$ (Table 4). The upper limit for the column density of $CH_3OH$ toward the Main source was calculated assuming a $T_{rot}$ of 51 K (to match the temperature of $H_2CO$ toward Main) and a line width of 0.7 km s$^{-1}$. The inferred dust temperatures are significantly lower than the sublimation temperature of $CH_3OH$ (Penteado et al. 2017) and so the observed methanol is likely being produced by ice sputtering in shock waves.

## 4. Discussion

### 4.1. Physical Origin of Outflow Emission

The CO emission has multiple spatially overlapping components indicating that the outflow is nearly perpendicular to the line of sight. The shape of the redshifted emission in CO and $^{13}$CO to the southwest of the continuum source implies that there is a dense clump of molecular gas diverting the outflowing material, which is traced in our observations by $H_2CO$ and $CH_3OH$. This is also suggested in Maureira et al. (2020) in maps of $NH_2D$. The alternative scenario is that this S-shaped emission and slower, more distant blueshifted emission indicates a precessing outflow. The broad redshifted emission to the northeast of the continuum may originate from a second source implying a tight binary system within the continuum. There is no corresponding blueshifted broad component detected at similar velocities but it may have been disrupted by the molecular clump south of the continuum source. The irregular velocity structure demonstrates that in the early stages of star formation, the outflow launching is chaotic. The clumpy structure observed in CS and $H_2CO$ emission may be due to small ejections from the early stages of the stellar outflow or simply the clumpiness of the surrounding cloud. The underlying power source driving the outflow activity associated with Cha-MMS1 could be either a single precessing outflow or two outflows from a close binary system. Alternative scenarios can also produce outflow precession, for instance, the misalignment between the outflow axis (a proxy for angular momentum axis) and the magnetic field axis as discussed in Busch et al. (2020), which does not require a binary. Similarly, a change in the angular momentum axis of the infalling material due to turbulent conditions can also produce shape distortions (Matsumoto et al. 2017).

### 4.2. Status of Cha-MMS1

While many FHSC candidates have been proposed over the past 20 yr, most have now been identified as young class 0 objects, VeLLOs, or prestellar cores. Compared to the outflow properties of the remaining FHSC candidates with published outflow properties (G208.89-20.04, Dutta et al. 2022; MC35-mm (I1535-NE), Fujishiro et al. 2020; L1451-mm, Pineda et al. 2011; and GF 9-2, Furuya et al. 2019), Cha-MMS1 has a similar maximum velocity range, generally lower dynamical time, and higher mechanical luminosity (by at least two orders of magnitude). The mechanical luminosity is also several orders of magnitude higher than the VeLLOs identified in Dunham et al. (2011). The sources with the most similar outflow properties are the young stars in Barnard 1b (Hirano & Liu 2014). Numerous complex molecular lines have been detected toward B1b-S (Marcelino et al. 2018), indicating that it is too evolved to be an FHSC.

#### 4.2.1. Mechanical Properties

The mechanical properties we have derived for Cha-MMS1 are several orders of magnitude lower than a 1 $L_\odot$ star and are in line with the relationships between mass and luminosity and momentum rate and luminosity shown in Wu et al. (2004). The line-of-sight outflow properties we calculated using the CO (2-1) transition are generally similar to the values in Busch et al. (2020), which were calculated using the CO (3-2) transition. They concluded that Cha-MMS1 was not an FHSC, though it was one of the youngest Class 0 objects ever detected. We find the dynamical time to be on the order of hundreds of years, rather than thousands, which results in our time-dependent values being an order of magnitude higher. We agree with their assessment that the bent shape of the redshifted emission in CO and $^{13}$CO to the southwest of the continuum source is likely due to the clump of molecular material there.

In Figure 10, we compare the mechanical outflow properties for Cha-MMS1 and other former FHSC candidates from the literature. Of the literature sources and former FHSC candidates, Cha-MMS1 has the highest force and the second highest mechanical luminosity. The Cha-MMS1 outflows have higher values than similar low-luminosity sources for all mechanical properties. In many respects, the properties of Cha-MMS1 are similar to L673-7-IRS, a source that has been categorized as a VeLLO, while Cha-MMS1 appears to be a very young Class 0 object. However, a general conclusion from Figure 10 is that the outflow mechanical properties of both VeLLOs and low-luminosity Class 0 sources (which were former FHSC candidates) are spread over several orders of magnitude with no clear relationship with $L_{int}$.

#### 4.2.2. Chemistry

The chemistry of the Cha-MMS1 environment can be understood by assessing the relative importance of thermal desorption and sputtering in shock waves at each of the four regions identified: N, M, S, and W. For a balance between molecular accretion (sticking) and thermal desorption, the fraction of a molecule that is present in the gas relative to its total available abundance, $f_x$, is, e.g., Charnley et al. (2001)

$$f_x = \frac{1}{1 + \lambda_x/\xi_x}, \quad (1)$$

where the accretion rate, $\lambda_x$, is

$$\lambda_x = 4.55 \times 10^{-18} n_H \left(\frac{T}{M_x}\right)^{1/2} \quad \text{s}^{-1}, \quad (2)$$

with $T$ the gas temperature, $n_H$ the gas density, and $M_x$ the molecular weight of X. Here we have adopted a total surface area for the dust of $10^{-22}\pi$ cm$^2$ and unit sticking efficiency.

The desorption rate, $\xi_x$, is

$$\xi_x = \nu_X \exp\left[-\frac{E_x}{kT_{gr}}\right] \quad \text{s}^{-1}, \quad (3)$$

where $\nu_X$ is the vibrational frequency of X in a surface binding site, $E_x$ is the binding energy, and $T_{gr}$ is the grain temperature. In the following, we assume $T_{rot} \approx T \approx T_{gr}$ with $n_H = 3 \times 10^4$ cm$^{-3}$,

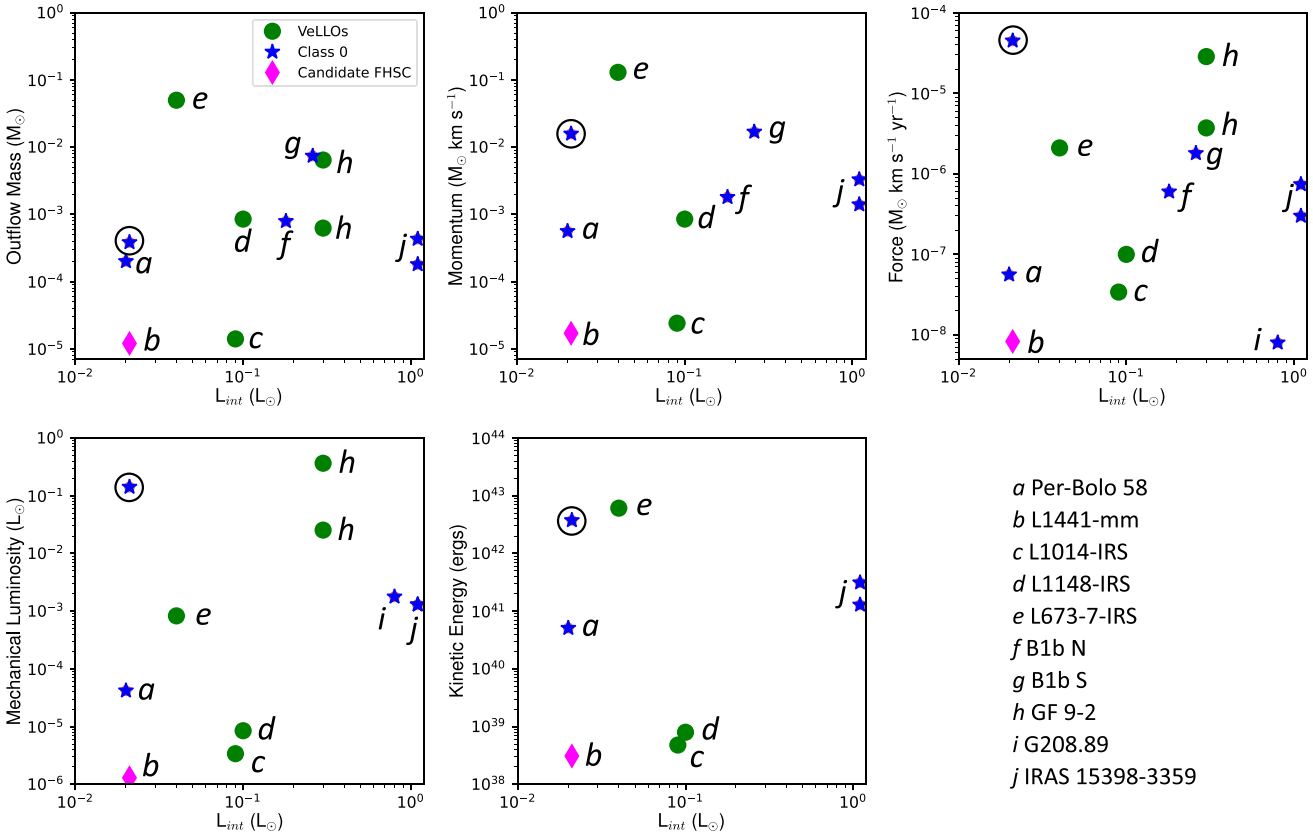


**Figure 10.** Comparing the mechanical outflow properties of former FHSC candidates from the literature. Cha-MMS1 is circled and properties are from this work. The objects labeled *a* to *j* are as follows: *a* Per-Bolo 58, *b* L1441-mm, *c* L1014-IRS, *d* L1148-IRS, *e* L673-7-IRS, *f* B1b-N, *g* B1b-S, *h* GF 9-2 (where there are two points representing outflows in 7 K and 22 K environments), *i* G208.89, and *j* IRAS 15398-3359 (where there are two points representing outflows in 25 K and 100 K environments). Outflow properties for points *a*-*e* are from Dunham et al. (2011), *f* and *g* are from Hirano & Liu (2014), *h* is from Furuya et al. (2019), *i* is from Dutta et al. (2022), and *j* is from Vazzano et al. (2021). Not all sources appear in all subplots as those properties are not reported in literature.

$\nu_X = 10^{12}$ s$^{-1}$ and binding energies from the UMIST database (McElroy et al. 2013): $E_{CH_3OH} = 4930$ K, $E_{H_2CO} = 2050$K and $E_{CS} = 1900$ K.

Using the $T_{rot}$ values in Table 3, we find that thermal desorption of $H_2CO$ accounts for $f_{H_2CO} \sim 100\%$ of the emission at M and N and ~70% at W; at S, $f_{H_2CO} \approx 0$ and so sputtering in shock waves is required. Since $E_{CS} \lesssim E_{H_2CO}$, adopting the same $T_{rot}$ values leads to the same conclusions for CS; this also explains the similar spatial distributions of the two molecules. For $CH_3OH$, the dust temperatures inferred from the $T_{rot}$ values in Table 4 yields $f_{CH_3OH} \approx 0$ at all four positions, ruling out thermal desorption and implying that the emission observed at N, S, and W arises from ice sputtering in shock interactions with the outflowing material.

Therefore we conclude:

1. At S, all three molecules have been sputtered from ices in shocks.
2. At M, $H_2CO$ and CS have been thermally desorbed and the absence of methanol emission attests to no discernible shock activity.
3. At N and W, although thermal desorption alone could explain the presence of $H_2CO$ and CS, the association with outflow lobes and $CH_3OH$ emission strongly suggests that they are also the products of sputtering.

We can compare the chemical structure of Cha-MMS1 with other sources at early stages of evolution. IRAS 15398-3359 (hereafter I15398) is a VeLLO/class 0 protostar and was identified as a prototype warm carbon-chain source (WCCS; Sakai & Yamamoto 2013) as it contains a diverse array of interstellar carbon-chain molecules previously only identified in cold molecular clouds (e.g., TMC-1). While the envelope of Cha-MMS1 is similarly rich in carbon-chain molecules (Cordiner et al. 2012), they are located in cold gas and the nondetection of $HC_3N$ reported here suggests that the central protostellar region is depleted in carbon chains.

I15398 is more luminous than Cha-MMS1 and contains well-developed outflows, consistent with it being at a later evolutionary stage. As with Cha-MMS1, $H_2CO$ is detected in the outflows and a shock origin has been suggested (Okoda et al. 2020). However, unlike Cha-MMS1, the $CH_3OH$ emission is more compact and associated with a continuum peak. The recent detection of $HCOOCH_3$ and $CH_2DOH$ further indicates that ice mantle disruption has occurred and a hot corino has formed (Okoda et al. 2023). By contrast, dust temperatures throughout Cha-MMS1 are too low for $CH_3OH$ evaporation. Thus, MMS1 cannot be classified as either a WCCC or a hot corino (or a hybrid of these); its kinematic characteristics and chemistry indicates a much earlier evolutionary state.

L1451-mm is a source at an earlier evolutionary stage with respect to Cha-MMS1. Its very low luminosity, the presence of a slow outflow, compact dust emission, and outflow properties (Figure 10) have led to L1451-mm being previously identified

as an FHSC candidate (Pineda et al. 2011). Recent molecular line observations (Wakelam et al. 2022), including the detection of $CH_3OH$ maser emission and SiO, allow the chemistry of the L1451-mm protostellar environment to be compared to Cha-MMS1. Interferometric (NOEMA) maps show that strong emission from $H_2CO$ and CS is present and has both compact and extended components, similar to that observed in Cha-MMS1. However, the emissions from $CH_3OH$ and $HC_3N$ only peak at the compact continuum position and, with the detection of SiO, clearly indicates shock activity near the protostar, in contrast to what is observed at position M in Cha-MMS1. Wakelam et al. (2022) ruled out L1451-mm being an FHSC based on the inability of shocks produced in FHSC outflow models to account for the observed SiO and $CH_3OH$ abundances.

Thus, compared to Cha-MMS1, the chemistry in L1451-mm would appear to suggest that it is at a later evolutionary stage, at variance with it being relatively youthful, as determined from its physical state (Figure 10). It is difficult to reconcile its apparently more evolved chemical composition with L1451-mm being younger than Cha-MMS1 since one would expect that the higher luminosity and more energetic outflows (Figure 10) would favor more efficient thermal desorption and sputtering of ice mantles in Cha-MMS1.

One possibility is that the chemistry of these sources is governed by the physics associated with episodic accretion due to luminosity outbursts, where cooling grains can recondense molecules from the gas. Adopting the (UMIST) binding energies for SiO (3500 K) and $HC_3N$ (4580 K), and $T_{\rm rot} = 51$ K, these molecules would also be sequestered in ices at position M. A previous higher luminosity outburst with accompanying mantle evaporation, has been suggested as the origin of the cold methanol detected in the Cha-MMS1 envelope (Cordiner et al. 2012). Thus, it may be that M is at the end of an episodic recondensation event where the more refractory molecules are on the dust but where the outflows are still chemically active. L1451-mm, on the other hand, may be at the start of such a phase.

## 5. Conclusions

We observed Cha-MMS1 with ALMA in Band 6 at high angular resolution and detected $^{12}CO$ and $^{13}CO$ emission as well as CS, $H_2CO$, and $CH_3OH$. We find a weak outflow nearly perpendicular to the line of sight toward the northeast and southwest of the continuum source. The effects of the outflow are seen on the local molecular cloud through CS, $H_2CO$, and $CH_3OH$ emission. A kink in the southwestern outflow corresponds with low rotational temperature ($\sim$20–30 K) emission from $H_2CO$ and $CH_3OH$ indicating a clump of molecular material being shocked by the outflow.

Comparison of Cha-MMS1 with other low-luminosity protostars supports the view that it is not a viable FHSC. In fact, recent observations of SiO and $CH_3OH$ in L1451-mm (Wakelam et al. 2022) suggest that it too is not an FHSC. The weak outflow and relatively low temperatures associated with this object indicate that it is one of the youngest known Class 0 objects.

## Acknowledgments

This paper makes use of the following ALMA data: ADS/JAO.ALMA 2013.1.01113.S. ALMA is a partnership of ESO (representing its member states), NSF (USA), and NINS (Japan), together with NRC (Canada) and NSC and ASIAA (Taiwan), in cooperation with the Republic of Chile. The Joint ALMA Observatory is operated by ESO, AUI/NRAO, and NAOJ. The National Radio Astronomy Observatory is a facility of the National Science Foundation operated under a cooperative agreement by Associated Universities, Inc. V.A.'s research for this article was supported by an appointment to the NASA Postdoctoral Program at the NASA Goddard Space Flight Center, administered by Universities Space Research Association under contract with NASA. V.A. is currently supported by an NWO Veni grant number VI.Veni.202.135. V. A., M.C., and S.C. were supported by the NASA Planetary Science Division Internal Scientist Funding Program through the Fundamental Laboratory Research work package (FLaRe).

*Facility:* ALMA.

## Appendix A
## Spectra

The regions in Figure 11 depict the spectral extraction locations for Figures 12–15.

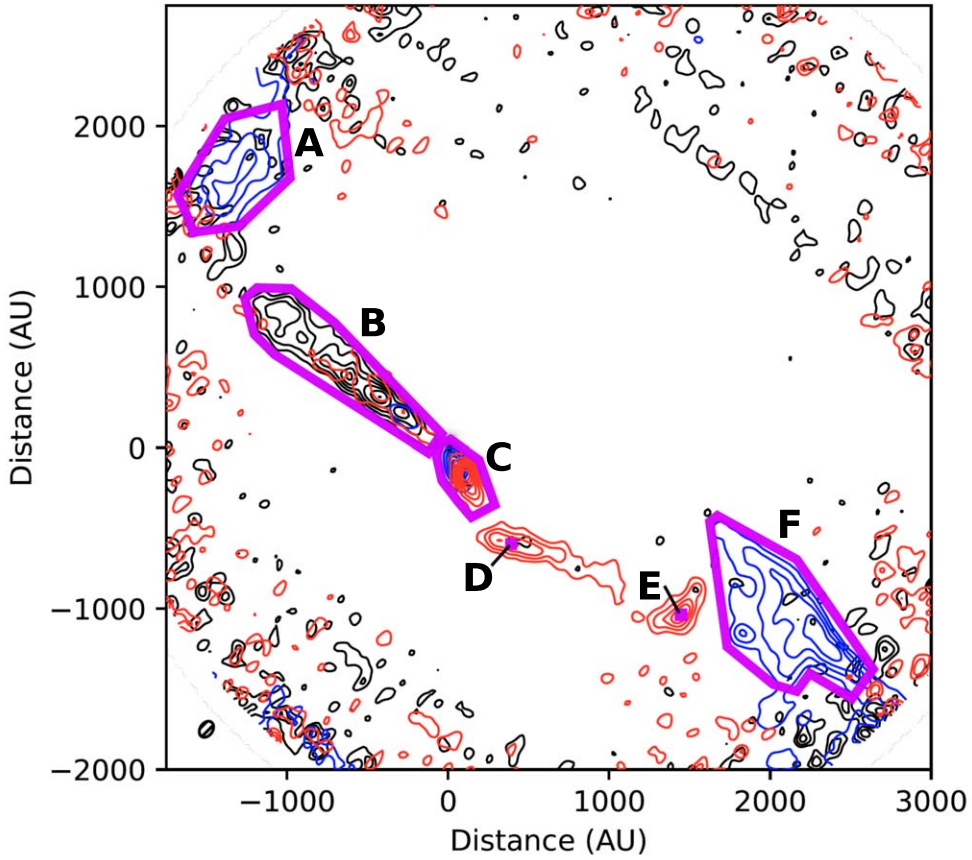


**Figure 11.** Integrated intensity maps of CO as in Figure 5 with subregions labeled A-F. All spectra are integrated over the area surrounded in magenta, except D and E which are taken from the emission peak.

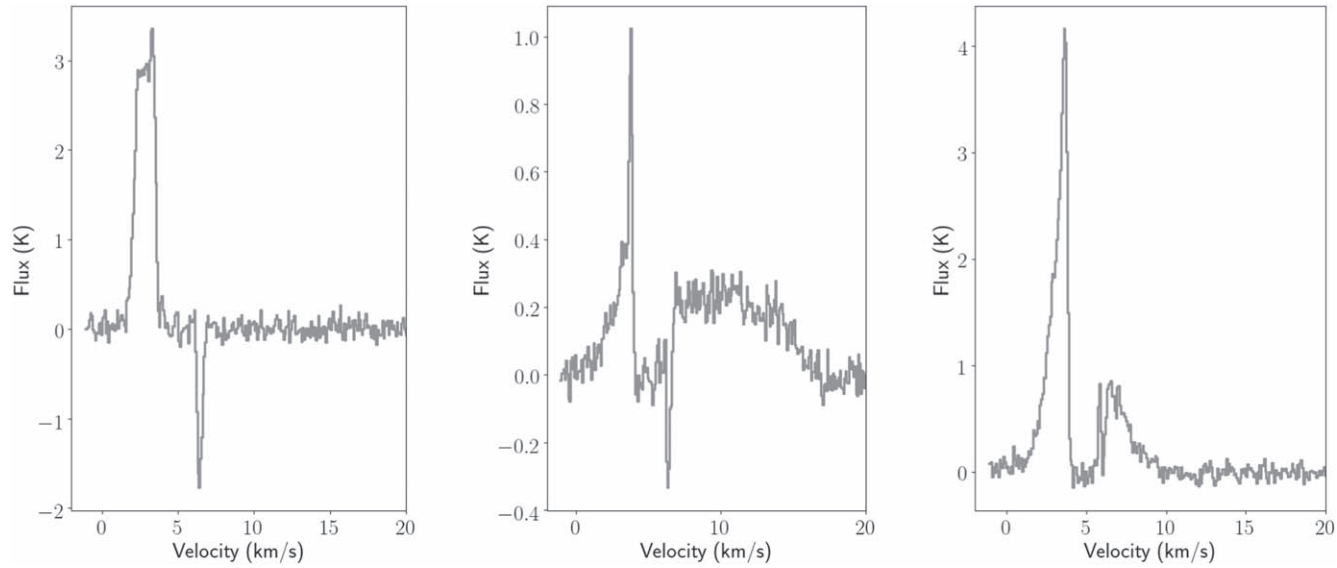


**Figure 12.** CO spectra toward subregions A, B, and C (left to right) from Figure 11.

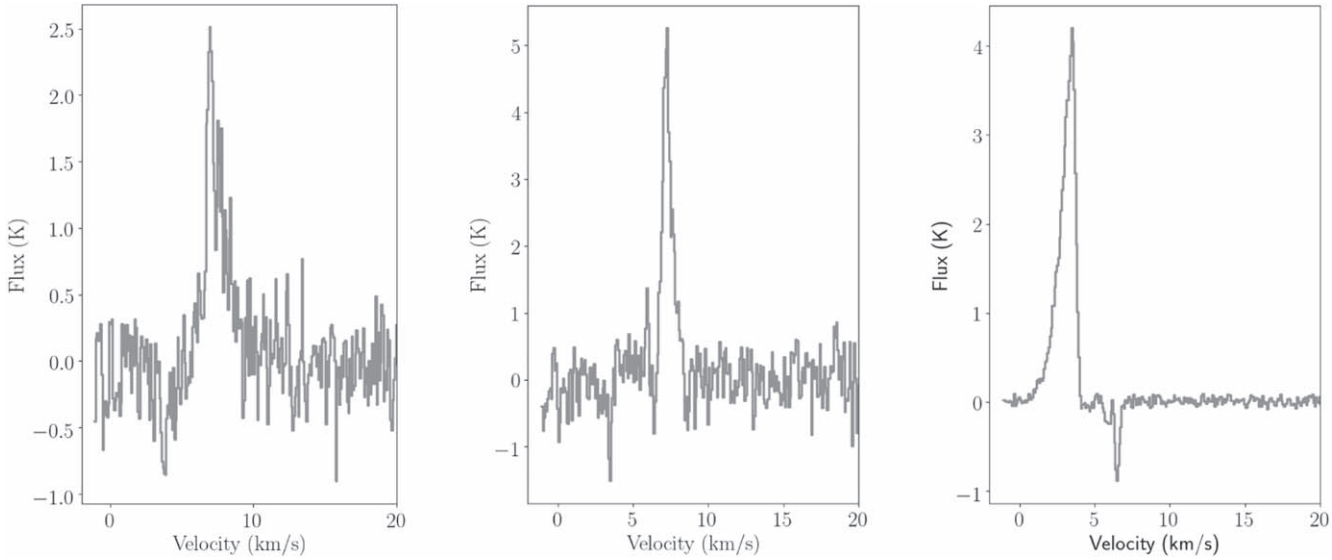


**Figure 13.** CO spectra toward subregions D, E, and F (left to right) from Figure 11.

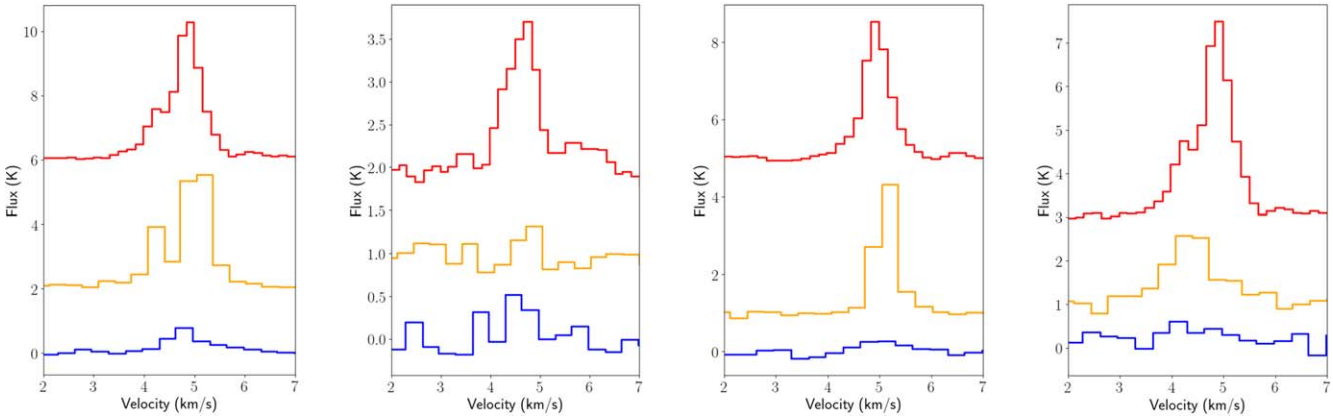


**Figure 14.** $H_2CO$ spectra toward each subregion (left to right): Main, N, S, and W. Red (top) corresponds to 3(0,3)-2(2,1) (218222 MHz); yellow (middle) corresponds to 3(1,2)-2(1,1) (225698 MHz); and blue (bottom) corresponds to 3(0,3)-2(2,1) (218475 MHz).

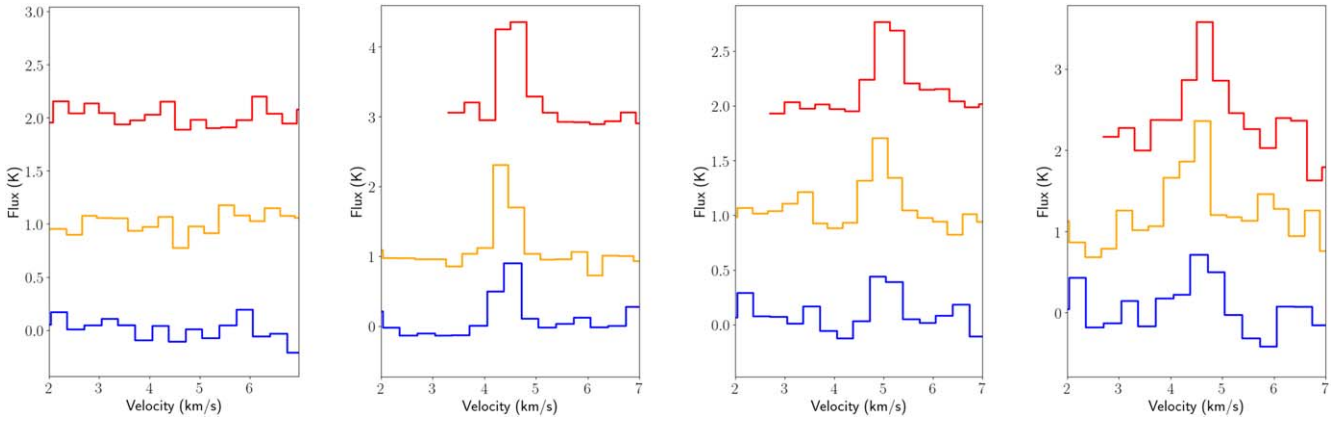


**Figure 15.** $CH_3OH$ spectra toward each subregion (left to right): Main, N, S, and W. Red (top) corresponds to 5(0,5)-4(0,4)++ (241791 MHz); yellow (middle) corresponds to 5(-1,5)-4(-1,4) (241767 MHz); and blue (bottom) corresponds to 5(3,2)-4(3,1) (218440 MHz). $CH_3OH$ emission is clearly not detected toward the Main source.

## Appendix B
## Additional Integrated Intensity Maps

The integrated intensity maps included here (Figures 16 and 17) demonstrate the localization of $H_2CO$ and $CH_3OH$ emission in the vicinity of Cha-MMS1.

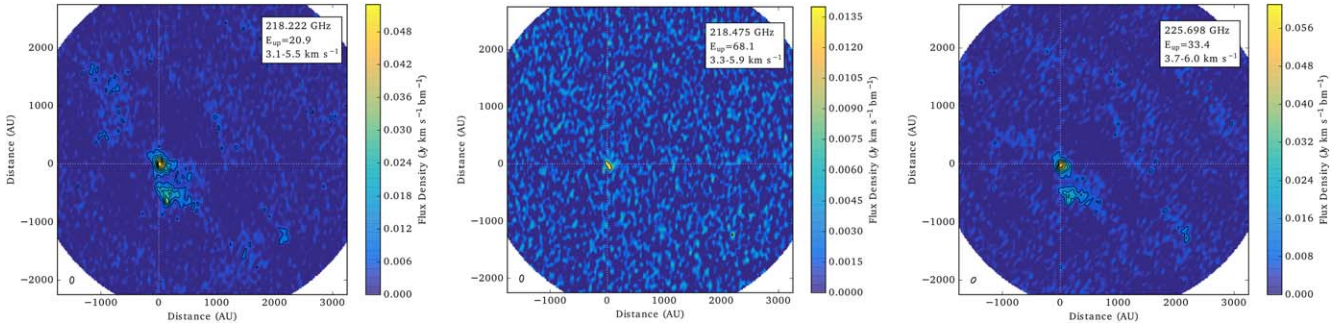


**Figure 16.** Primary beam-corrected integrated intensity maps for $H_2CO$ transitions at (left) 218.222 GHz (between 3.1 and 5.5 km s$^{-1}$); (middle) 218.475 GHz (between 3.3 and 5.9 km s$^{-1}$); and (right) 225 GHz (between 3.7 and 6.0 km s$^{-1}$). The continuum peak is located at 0, 0 au and is indicated by the intersection of the dotted lines. Left: contours start at $3\sigma$ ($\sigma = 2.1$ mJy beam$^{-1}$ km s$^{-1}$) continue in intervals of $3\sigma$ to a peak of 53 mJy beam$^{-1}$ km s$^{-1}$. The beam size is $0\farcs80 \times 0\farcs43$. Middle: contours start at $3\sigma$ ($\sigma = 3.1$ mJy beam$^{-1}$ km s$^{-1}$) and continue in intervals of $3\sigma$ to a peak of 14 mJy beam$^{-1}$ km s$^{-1}$. The beam size is $0\farcs81 \times 0\farcs45$. Right: contours start at $3\sigma$ ($\sigma = 3.5$ mJy beam$^{-1}$ km s$^{-1}$) and continue in intervals of $3\sigma$ to a peak of 61 mJy beam$^{-1}$ km s$^{-1}$. The beam size is $0\farcs72 \times 0\farcs44$.

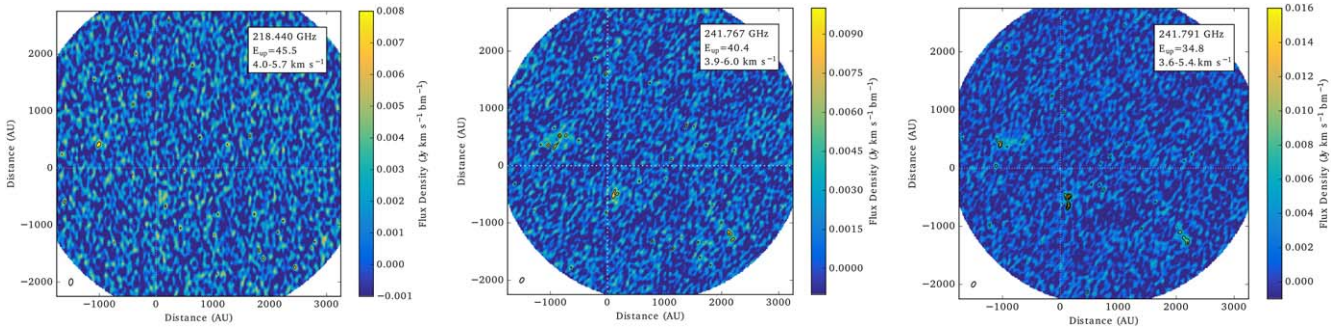


**Figure 17.** Primary beam-corrected integrated intensity maps for $CH_3OH$ transitions at (left) 218.440 GHz (between 4.0 and 5.7 km s$^{-1}$); (middle) 241.767 GHz (between 3.9 and 6.0 km s$^{-1}$); and (right) 241.791 GHz (between 3.6 and 5.4 km s$^{-1}$). The continuum peak is located at (0, 0) au and is indicated by the intersection of the dotted lines. Left: contours start at $3\sigma$ ($\sigma = 2.8$ mJy beam$^{-1}$) continue in intervals of $1\sigma$ to a peak of 7.3 mJy beam$^{-1}$. The beam size is $0\farcs81 \times 0\farcs45$. Middle: contours start at $3\sigma$ ($\sigma = 2.7$ mJy beam$^{-1}$) continue in intervals of $1\sigma$ to a peak of 9.5 mJy beam$^{-1}$. The beam size is $0\farcs68 \times 0\farcs40$. Right: contours start at $3\sigma$ ($\sigma = 2.7$ mJy beam$^{-1}$) and continue in intervals of $1\sigma$ to a peak of 16 mJy beam$^{-1}$. The beam size is $0\farcs68 \times 0\farcs40$.

## ORCID iDs

Veronica Allen https://orcid.org/0000-0002-8021-0344
Martin A. Cordiner https://orcid.org/0000-0001-8233-2436
Steven B. Charnley https://orcid.org/0000-0001-6752-5109
Yi-Jehng Kuan https://orcid.org/0000-0002-4336-0730
Eva Wirström https://orcid.org/0000-0002-0656-876X

## References

Bate, M. R., Tricco, T. S., & Price, D. J. 2014, MNRAS, 437, 77
Belloche, A., Parise, B., van der Tak, F. F. S., et al. 2006, A&A, 454, L51
Belloche, A., Schuller, F., Parise, B., et al. 2011, A&A, 527, A145
Benedettini, M., Viti, S., Codella, C., et al. 2013, MNRAS, 436, 179
Bhandare, A., Kuiper, R., Henning, T., et al. 2018, A&A, 618, A95
Bolatto, A. D., Wolfire, M., & Leroy, A. K. 2013, ARA&A, 51, 207
Busch, L. A., Belloche, A., Cabrit, S., et al. 2020, A&A, 633, A126
Charnley, S. B., Rodgers, S. D., & Ehrenfreund, P. 2001, A&A, 378, 1024
Cordiner, M. A., Charnley, S. B., Wirström, E. S., et al. 2012, ApJ, 744, 131
Dunham, M. M., Chen, X., Arce, H. G., et al. 2011, ApJ, 742, 1
Dunham, M. M., Crapsi, A., Evans, N. J. I., et al. 2008, ApJS, 179, 249
Dutta, S., Lee, C.-F., Hirano, N., et al. 2022, ApJ, 931, 130
Dzib, S. A., Loinard, L., Ortiz-León, G. N., et al. 2018, ApJ, 867, 151
Friesen, R. K., Pon, A., Bourke, T. L., et al. 2018, ApJ, 869, 158
Fujishiro, K., Tokuda, K., Tachihara, K., et al. 2020, ApJL, 899, L10
Furuya, R. S., Kitamura, Y., & Shinnaga, H. 2019, ApJ, 871, 137
Goldsmith, P. F. 2001, ApJ, 557, 736
Goldsmith, P. F., & Langer, W. D. 1999, ApJ, 517, 209
Hiramatsu, M., Hayakawa, T., Tatematsu, K., et al. 2007, ApJ, 664, 964
Hirano, N. 2019, in ALMA2019: Science Results and Cross-Facility Synergies, 90
Hirano, N., & Liu, F.-c. 2014, ApJ, 789, 50
Koumpia, E., van der Tak, F. F. S., Kwon, W., et al. 2016, A&A, 595, A51
Ladd, E. F., Wong, T., Bourke, T. L., & Thompson, K. L. 2011, ApJ, 743, 108
Larson, R. B. 1969, MNRAS, 145, 271
López-Sepulcre, A., Cesaroni, R., & Walmsley, C. M. 2010, A&A, 517, A66
López-Sepulcre, A., Codella, C., Cesaroni, R., Marcelino, N., & Walmsley, C. M. 2009, A&A, 499, 811
Machida, M. N., Inutsuka, S.-i., & Matsumoto, T. 2008, ApJ, 676, 1088
Marcelino, N., Gerin, M., Cernicharo, J., et al. 2018, A&A, 620, A80
Masson, J., Chabrier, G., Hennebelle, P., et al. 2016, A&A, 587, A32
Masunaga, H., & Inutsuka, S.-i. 2000, ApJ, 531, 350
Matsumoto, T., Machida, M. N., & Inutsuka, S. I. 2017, ApJ, 839, 69
Maureira, M. J., Arce, H. G., Dunham, M. M., et al. 2020, MNRAS, 499, 4394
McElroy, D., Walsh, C., Markwick, A. J., et al. 2013, A&A, 550, A36
Okoda, Y., Oya, Y., Francis, L., et al. 2023, ApJ, 948, 127
Okoda, Y., Oya, Y., Sakai, N., et al. 2020, ApJ, 900, 40
Penteado, E. M., Walsh, C., & Cuppen, H. M. 2017, ApJ, 844, 71
Pineda, J. E., Arce, H. G., Schnee, S., et al. 2011, ApJ, 743, 201
Price, D. J., Tricco, T. S., & Bate, M. R. 2012, MNRAS, 423, L45
Reipurth, B., Nyman, L. A., & Chini, R. 1996, A&A, 314, 258

Saigo, K., & Tomisaka, K. 2011, ApJ, 728, 78
Sakai, N., & Yamamoto, S. 2013, ChRv, 113, 8981
Sánchez-Monge, Á., López-Sepulcre, A., Cesaroni, R., et al. 2013, A&A, 557, A94
Spear, S., Maureira, M. J., Arce, H. G., et al. 2021, ApJ, 923, 231
Tomida, K., Okuzumi, S., & Machida, M. N. 2015, ApJ, 801, 117
Tomida, K., Tomisaka, K., Matsumoto, T., et al. 2010, ApJ, 714, L58
Tsitali, A. E., Belloche, A., Commerçon, B., et al. 2013, A&A, 557, A98
Väisälä, M. S., Harju, J., Mantere, M. J., et al. 2014, A&A, 564, A99
Vastel, C., Bottinelli, S., Caux, E., et al. 2015, in SF2A-2015: Proc. of the Annual Meeting of the French Society of Astronomy and Astrophysics, ed. F. Martins et al. (Société Française d'Astronomie et d'Astrophysique), 313
Vazzano, M. M., Fernández-López, M., Plunkett, A., et al. 2021, A&A, 648, A41
Wakelam, V., Coutens, A., Gratier, P., et al. 2022, A&A, 666, A191
Wu, Y., Wei, Y., Zhao, M., et al. 2004, A&A, 426, 503
Young, A. K. 2023, FrASS, 10, 1288730
Zhang, Y., Higuchi, A. E., Sakai, N., et al. 2018, ApJ, 864, 76